JOURNAL OF GEOPHYSICAL RESEARCH, VOL. 98, NO. D3, PAGES 4931–4950, MARCH 20, 1993

The Earth's Radiation Budget and Its Relation to Atmospheric Hydrology 3. Comparison of Observations Over the Oceans With a GCM

GRAEME L. STEPHENS, DAVID A. RANDALL, IAN L. WITTMEYER, AND DONALD A. DAZLICH

Department of Atmospheric Science, Colorado State University, Fort Collins

STEPHEN TJEMKES

Institute of Meteorology and Oceanography, State University of the Netherlands, Utrecht

This paper reports on a study that seeks to examine a very limited set of interactions between the hydrological cycle and the radiative processes that take place on Earth and attempt to test how well these interactions are simulated by a general circulation model. Two broad types of tests of the model are introduced in this paper. The first focuses on comparing various sensitivity relationships established by the model with those observed on Earth. The specific relationships examined in this paper include the sensitivities of column-integrated water vapor, the clear sky greenhouse effect, cloud albedo, and cloud radiative forcing to sea surface temperature. The second type of test focuses on comparison of simulated and observed seasonal cycles of the greenhouse effect and cloud radiative forcing. The main results of this study suggest that the model studied, which we take to be representative of the current generation of global climate models, is able to simulate some aspects of the observed sensitivities fairly well. Qualitative successes of the simulations include realistic variations of column vapor with sea surface temperature, the clear sky greenhouse parameter and its variation with both column vapor and sea surface temperature, and cloud longwave radiative forcing with sea surface temperature, as well as the seasonal changes of the greenhouse effect and the cloud radiative forcing. However, there exist many serious quantitative differences between the model and the observations. These include problems in the simulations of the column vapor in the tropics and an excessively strong clear-sky greenhouse effect in the mid-latitudes. These differences combine in such a way that the model underestimates the sensitivity of the clear-sky greenhouse to changes in sea surface temperature compared to that derived from observations. Significant differences between the simulated and the observed radiative properties of clouds include the overprediction of the longwave cloud radiative forcing over warm tropical oceans and a significant underestimate of the cloud reflection in mid-latitudes during the summer season.

1. INTRODUCTION

Numerical models of the global climate serve an important function in our attempts to study and understand the Earth's climate and any impending change of climate. One application of these models is as investigative tool to study the interaction of various physical processes in the model with the hope that we might gain insight into how these processes actually operate in the real world. Before we can attach any credibility to these models as a research tool, let alone as a predictive tool, it is crucial that they be evaluated by comparing them with suitable observational data. Unfortunately, this is not a simple task. It is relatively straight forward to simulate distributions of selected quantities, like surface temperature or the top of the atmosphere Earth radiation budget (ERB), and then compare these with observations. These tend to be sterile tests of the models and, while necessary and important first steps, by themselves offer little real clue as to which processes are poorly handled in the models and thus presumably poorly understood. Meaningful comparisons between model and observations are further complicated by the fact that it is virtually impossible to observe the key physical processes of the real climate system in isolation from other processes. It is even more difficult to test models under various scenarios of climate change since we cannot observe the climate of the future until that future arrives.

Stephens and Greenwald [1991*a*, *b*], hereafter referred to as part 1 and part 2 respectively, developed various procedures for analyzing satellite data to study both the greenhouse effect of the planet and the connections of water vapor and clouds to the ERB. The present paper adopts these procedures as well as others in an attempt to compare the Colorado State University (CSU) general circulation model (GCM) to observations over the global oceans. The latter are largely derived from satellite measurements. The main aim of the study reported here is to provide a limited test of how well one particular model treats certain interactions between its hydrological cycle and model parameterizations of radiative processes. Two broad types of tests of the model are introduced to study these interactions. The first type of test focuses on comparing various sensitivity relationships established in the model with those observed on Earth. These relationships are considered basic to our understanding of different climate feedbacks. For example, the existence of a relationship between the precipitable water content (PWC) and sea surface temperature (SST) is central to the existence of the water vapor feedback mechanism. If a model fails to reproduce such key observed sensitivities, then it cannot be trusted to simulate the important feedbacks correctly. The second type of test focuses on com-

Copyright 1993 by the American Geophysical Union.

Paper number 92JD02520.
0148-0227/93/92JD-0252$05.00

parison of the seasonal cycle of selected quantities. These comparisons are also important tests of the model under conditions of changing external forcing. If a model cannot simulate the seasonal cycle then it also lacks credibility as a tool for studying global climate.

The outline of this paper is as follows. A summary of the observational data used in this study is presented in section 2. Section 3 provides a brief description of the CSU GCM and summarizes the simulations carried out with this model. Section 4 describes a comparison of the modeled and observed precipitable water distributions and identifies important differences between these distributions. The clear sky greenhouse effect and its relation to these fields of water vapor is examined in section 5. It is shown how, as a result of differences in both the relationships between water vapor and SST and between the greenhouse effect and water vapor, the model's greenhouse sensitivity to SST is significantly smaller than that observed. The effects of clouds on the Earth's radiation budget are addressed in section 6 where comparisons of simulated and observed seasonal cycles of these effects are also discussed. The results of this study and the conclusions drawn from it are given in the final section 7 of the paper.

2. DATA

Details of some of the observational data used in this study are provided in parts 1 and 2. Earth radiation budget (ERB) data from two sources were used in these earlier studies: the narrow field-of-view, broadband scanning radiometer data of Nimbus 7 for the 1979 calendar year and the broadband scanning data of the Earth radiation budget experiment (ERBE) for the 1985 calendar year, whereas the present study uses only ERBE data. The ERBE data consist of daily flux data combined from the ERBS (Earth Radiation Budget Satellite) and NOAA-9 and NOAA-10 satellites which are processed to monthly averages for 1988 and details of these data are described by *Harrison et al.* [1990] in some detail. In this study, in contrast to parts 1 and 2, both ERBE data and the passive microwave measurements obtained from the Defense Military Satellite Program's (DMSP'S) special sensor microwave imager (SSMI) instrument [*Hollinger et al.*, 1987] are combined to study the relationship between the Earth's radiation budget and water vapor. Three years of SSMI data, 1988, 1989, and 1990, are used in the analyses described below. The retrieval of PWC from the SSMI data as used in this study follows the methodology discussed by *Tjemkes et al.* [1991] but has been both modified and extended to account for and retrieve cloud liquid water path (LWP), (Greenwald et al., A physical retrieval of cloud liquid water over the global oceans using SSMI observations, submitted to *Journal of Geophysical Research*, 1992). Details of the retrieval of LWP from the SSMI and the relation between ERBE and SSMI LWP will be described in a future paper. The SST data are those provided by the National Meteorological Center for the same observational period of the Nimbus 7 data and the *Reynolds* [1988] data for the period beyond 1983.

The present study also compares the results obtained with the above data to the clear sky radiances obtained from the TIROS operational vertical sounder (TOVS) instrument flown on the polar orbiter NOAA satellites. We use only clear sky radiance data from the 7.3-μm and 6.7-μm water vapor channels (channels 11 and 12, respectively). Characteristic weighting functions that convey the relative contributions to the emission at these wavelengths are presented in Figure 1. These weighting functions indicate how the channel 11 brightness temperatures are associated with emission from the middle troposphere, whereas the brightness temperatures of channel 12 correspond to emission by water vapor primarily in the middle and upper troposphere.

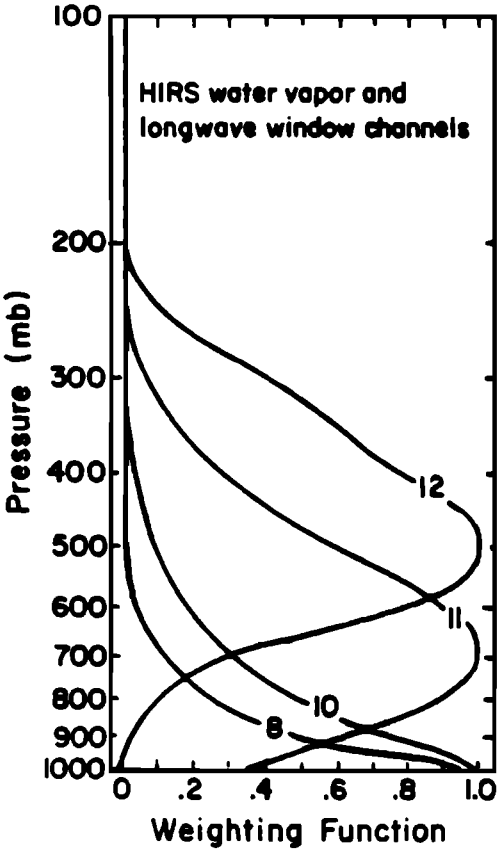

Fig. 1. Weighting functions of the TOVS water vapor channels 11 and 12.

The clear sky TOVS radiances used in this paper are those produced by the National Earth Satellite Service (NESS) and based on the algorithm of *McMillan and Dean* [1982]. Further details about the data, including the gridding and sampling techniques, as well as for a general description of the climatologies of channels 11 and 12, are presented by *Wu et al.* [1993]. January and July distributions of channels 11 and 12 brightness temperatures are presented in Figures 2*a* to 2*d*. These serve to highlight key features about the climatology of middle and upper tropospheric water vapor and correspond to the same months used in the analysis of SSMI data described below. We interpret the brightness temperature variations in the tropics and subtropics, regions where horizontal temperature gradients are relatively small, to be associated largely with variations in water vapor [*Wu et al.*, 1993]. For a given channel, higher brightness temperatures correspond to lower amounts of water vapor in the broad layer of the atmosphere specified by the weighting function. The January distributions of Figures 2*a* and 2*b*

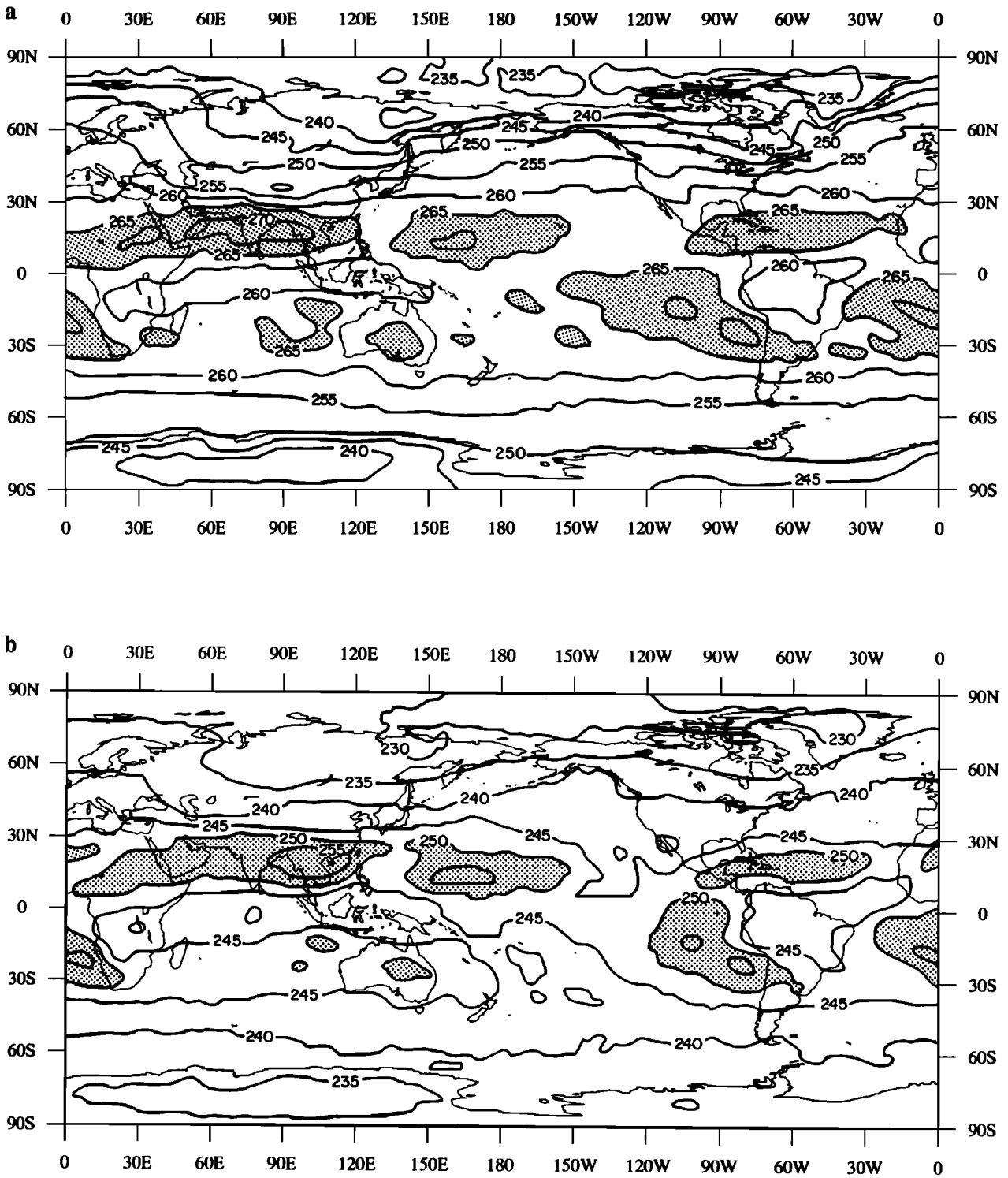

Fig. 2. Global distributions of (*a*) channel 11 and (*b*)channel 12 brightness temperatures for January. (*c*) and (*d*) same as (*a*) and (*b*) but for July.

show regions of high brightness temperature associated with regions of middle and upper tropospheric dryness extending out from the west coast of South America and across the northern reaches of the tropical Pacific Ocean. Other areas of dryness are associated with regions of subsidence over stratiform clouds off the west coasts of Africa, Australia, and from the west coast of California extending across the Pacific into the deep tropics. These dry regions are apparently also vertically coherent in the sense that the warmest temperatures of channel 11 coincide with the warmest temperatures of channel 12. The July maps in Figure 2*c* and 2*d* also demonstrate a similar coherence in the patterns of channels 11 and 12 although the actual brightness temperature distributions differ from those of January. The former shows

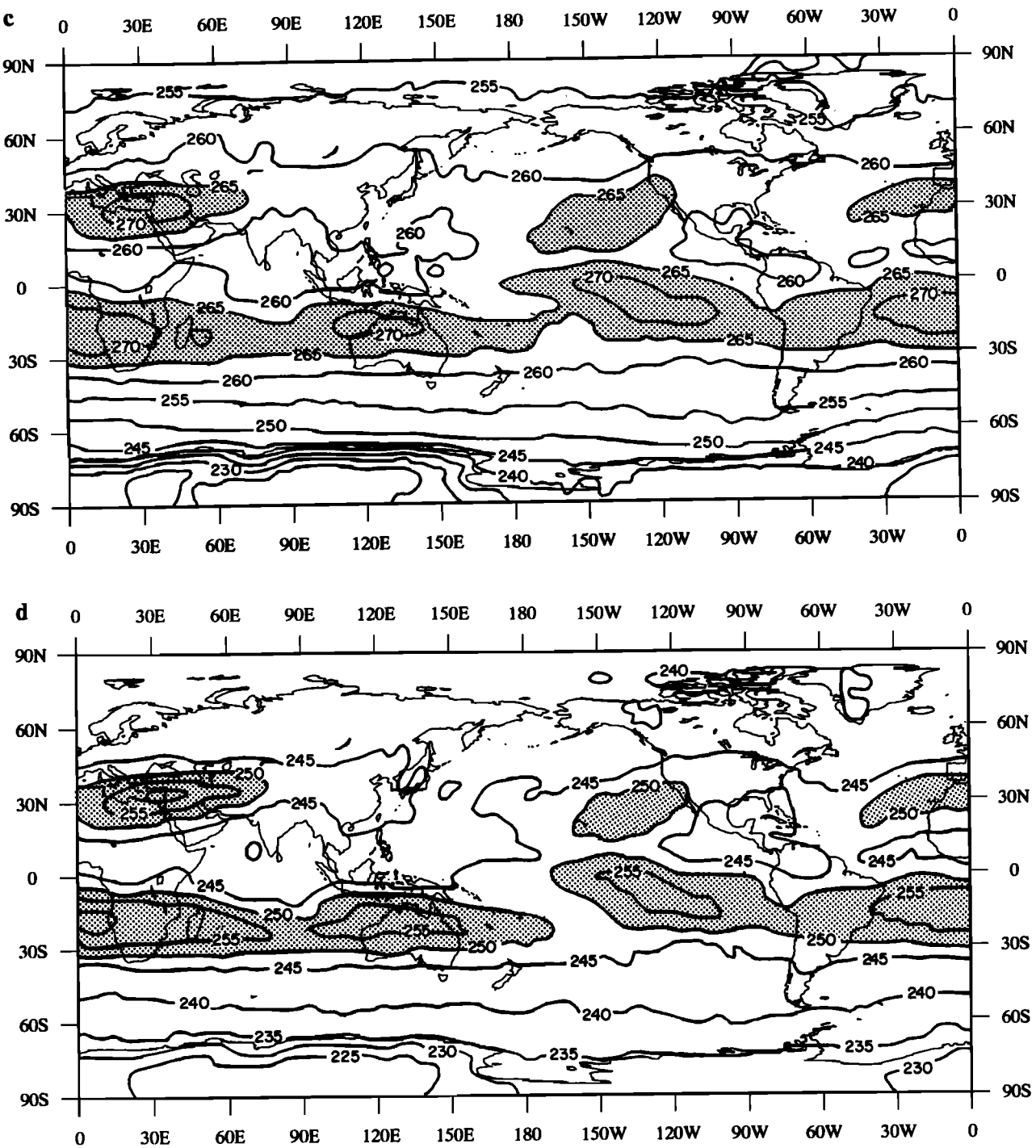

Fig. 2. (continued)

a more zonal pattern of dryness across the subtropics of the southern hemisphere associated with large-scale subsidence of the downward branch of the Hadley circulation.

3. The Colorado State University General Circulation Model (GCM)

The CSU GCM derives from the UCLA GCM which was developed at UCLA over a period of 20 years by A. Arakawa and collaborators. The changes to the original UCLA version of the model are discussed in other publications [e.g., *Randall et al.*, 1991]. The notable difference between the CSU GCM and the UCLA GCM is the improved parameterizations of radiation and cloud optical properties [*Harshvardhan et al.*, 1989] as well as new and extensive diagnostics as described by *Randall et al.* [1991].

In this paper the results are presented from a 2-year simulation. The resolution of the model is 4° latitude by 5° longitude, with 17 levels extending from the surface to 50 mbar. The dynamical time step is 450 s and the time step for other physical processes, including radiation, is 1 hour. The seasonally varying distribution of ground wetness is prescribed and monthly mean sea surface temperatures are used to interpolate to daily values at the lower boundary. The

experiment design is virtually the same as that described by *Randall et al.* [1991] and the model climatology is essentially identical to the climatology presented by *Randall et al.* [1985], *Harshvardhan et al.* [1989], and *Randall et al.* [1991]. The model results were sampled once per hour and daily means were derived from these hourly data and saved on a history tape. The daily means were subsequently averaged to produce the monthly averaged data used in this study.

4. Precipitable Water Comparisons

Passive microwave instruments flown on-board polar-orbiting satellites, such as the Scanning Multichannel Microwave Radiometer (SMMR) on Nimbus 7 and the SSMI on the DMSP satellites, provide excellent data for studying the vertically integrated water vapor (precipitable water) although so far only over the oceans. The extent that additional measurements, such as from the infrared channels of TOVS, provide information to complete the global coverage of this quantity remains a matter of research. Despite the limitation in the global extent of microwave data it is shown below how the PWC measured over the oceans is both a useful and an important data source for testing GCM simulations.

Figure 3 presents the monthly averaged PWC as a function of SST. The SSMI PWC values are represented by the cloud of points and correspond to monthly mean $1° \times 1°$ data for the 12 months of 1989. The 24 months of GCM PWC data, binned according to SST and averaged, are represented by the large circles in Figure 3, with the curves about these averages being one standard deviation above and below the mean. This format for comparing data and model-derived quantities is used hereafter throughout this paper. The characteristics of the observed relationship between PWC and SST have been discussed previously by *Stephens* [1990]. Whereas the broad characteristics of the observed relationship between PWC and SST are reproduced by the model, there exist important differences in detail. For example, the GCM is significantly drier than expected from observations over the warmest ocean waters (i.e., SST>300 K) and moister than the observations in regions defined by the range 288 K< SST < 300 K.

The characteristic differences between the model and the observations noted in Figure 3 are further illustrated by comparing of the distributions of PWC given in Figure 4*a* with those in Figure 4*b*. These distributions are the monthly mean PWC's for January and July respectively. The maps of Figure 4*a* are derived from the average of three January months of SSMI (1989, 1990, and 1991) and three July months (1988, 1989, and 1990), respectively, and the maps of Figure 4*b* are the average of two January and July simulations. The areas of high PWC in the SSMI distributions associated with the deep convection over the warm pool region of the West Pacific, the ITCZ, and the SPCZ all appear considerably drier in the model. We believe that this is a characteristic feature of the particular version of the *Arakawa and Schubert* [1974] convective parameterization scheme used in the model. *Cheng and Arakawa* [1991] also reach a similar conclusion and suggest that the dryness is due specifically to the failure of the parameterization to include the effects of convective downdrafts. Improvement of the parameterization to include these effects in the model is currently under development. The broad features of the observed distribution of PWC over the mid-latitude oceans are, on the whole, reasonably well reproduced by the model.

In the study of *Stephens* [1990] the parameter

$$r_w = \frac{w - \bar{w}}{w} \tag{1}$$

was introduced, where $\bar{w}$ is the value of PWC derived from a given value of SST based on an average of the data shown in Figure 3. The data used to derive $\bar{w}$ are given in Table 1. The virtue of this parameter is that it provides a direct measure of the effect of large-scale dynamics on PWC [*Stephens*, 1990]. For example, regions under the influence of moisture convergence and/or moist air advection are characterized by positive values of r_w, whereas regions of negative values of r_w suggest the influence of subsidence or dry air advection on the water vapor. *Stephens* [1990] mentions how maps of this factor reflect known characteristics of the time–mean large-scale circulation over the oceans. Maps of this parameter are presented in Plates 1*a* and 1*b* for averages of three Januarys and three Julys of SSMI data, respectively. Negative values of r_w correspond to areas of large-scale subsidence along the eastern flank of the subtropical anticyclonic circulation over the North Pacific and Atlantic Oceans in the January map of Plate 1*a*. Negative values of r_w also correspond to large-scale regions of subsidence associated with the Hadley circulation over the oceans of the southern

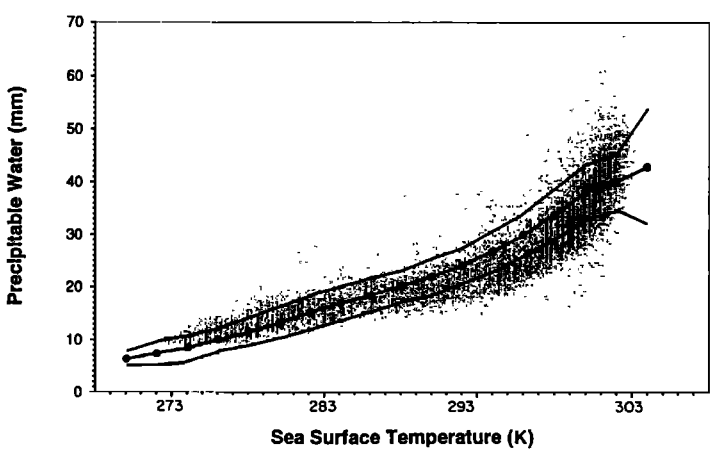

Fig. 3. Monthly averaged Precipitable Water Content (PWC) as a function of Sea Surface Temperature (SST). The Special Sensor Microwave Imager (SSMI) data are represented by the cloud of points and the model relationship by the middle curve. Curves on either side are one standard deviation about the mean PWC–SST model relationship.

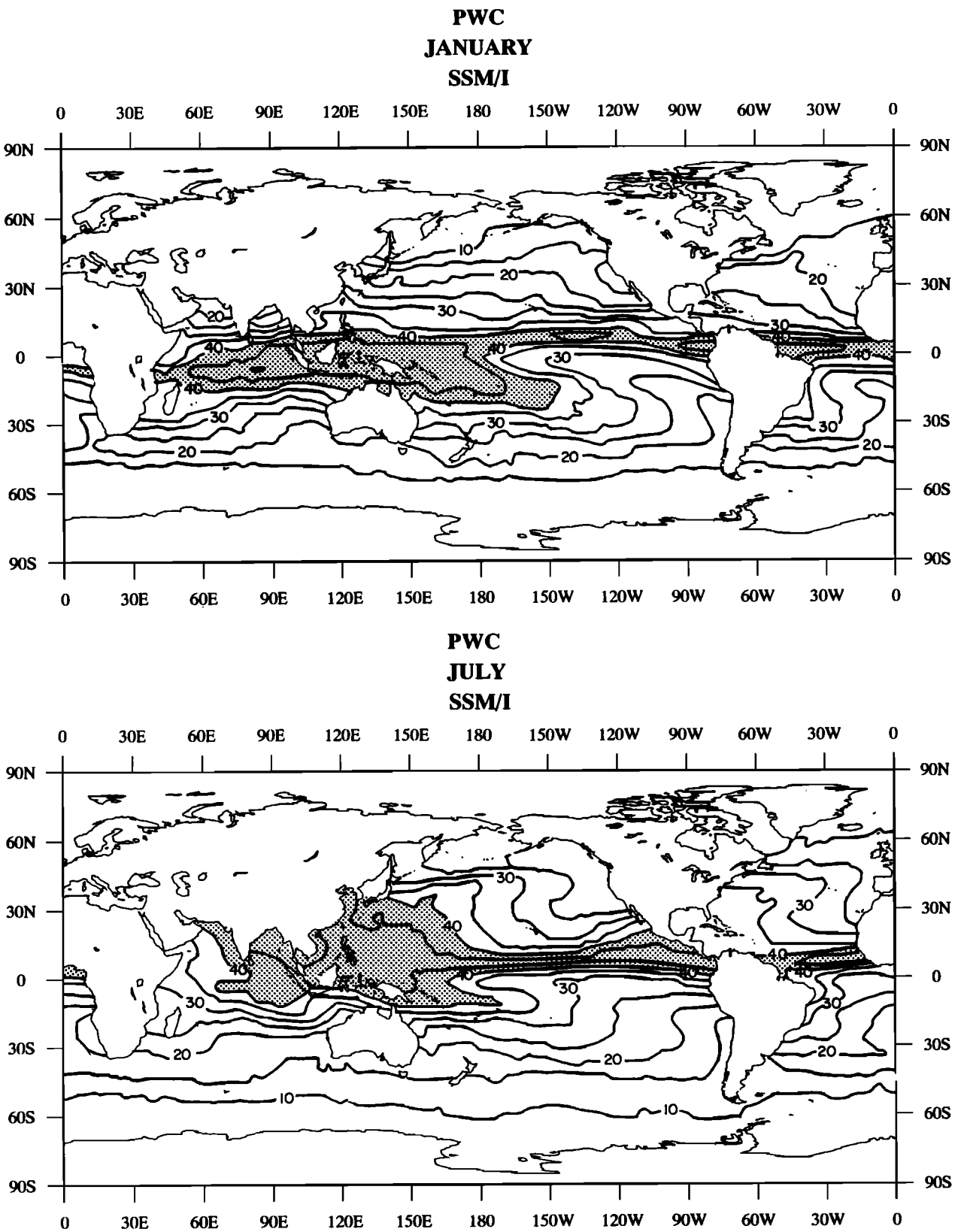

Fig. 4a. Monthly averaged PWCs derived from SSMI observations for (top) January and (bottom) July.

hemisphere during July. The effects of cold, dry air advection over the warmer Gulf and Kuroshio currents of the North Atlantic and Pacific oceans, respectively, produce regions of large negative values of this index during January in contrast to the positive values of r_w for these regions during July. The latter is indicative of convergence of moisture associated with the northward flux of moisture by transient eddies in these regions.

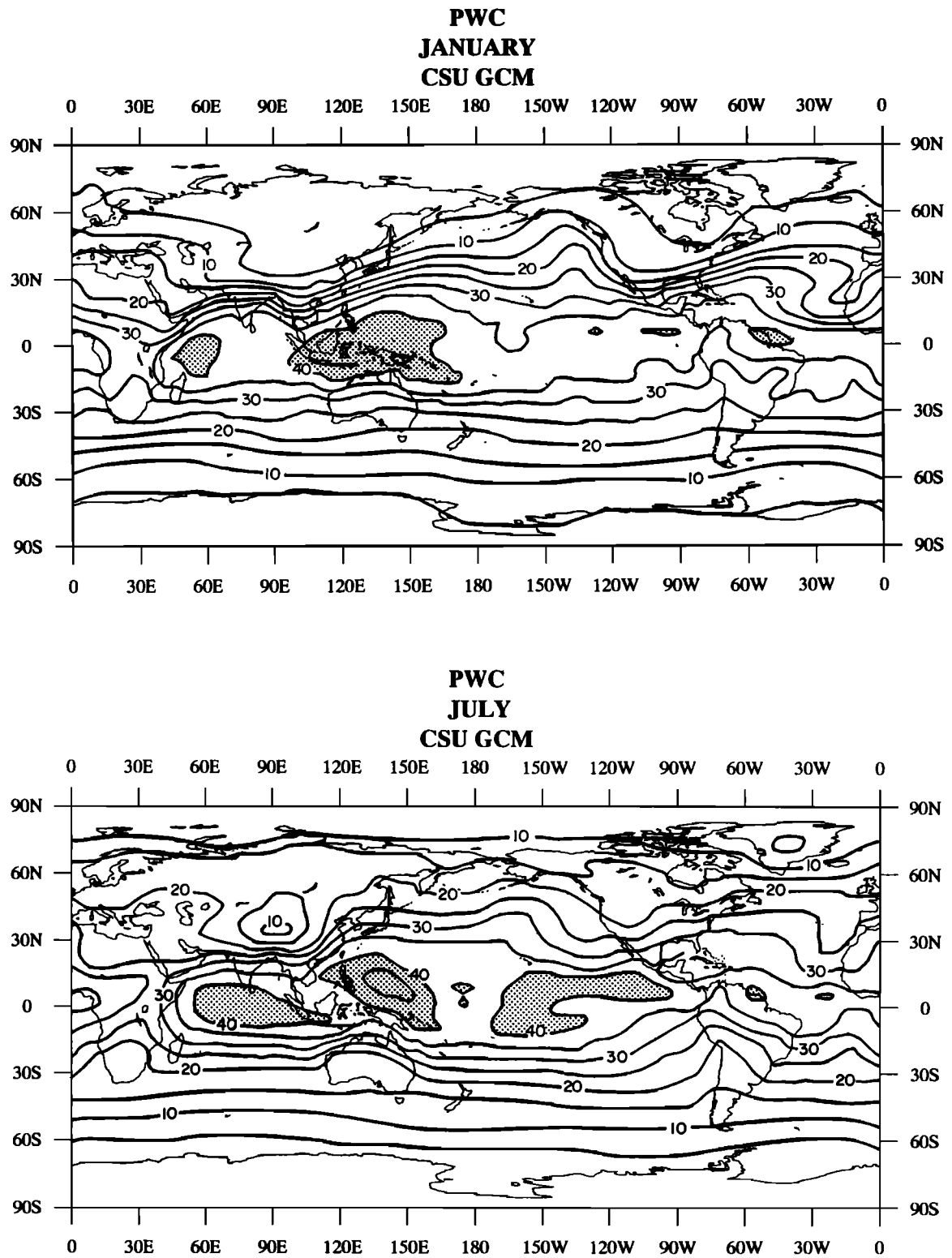

Fig. 4*b*. As in Figure 4*a* but for the General Circulation Model (GCM) PWC.

The corresponding January and July GCM distributions of r_w in Plates 2*a* and 2*b* are derived from the model's climatological PWC–SST relationship and not from the data given in Table 1. While the gross features associated with both dry and moist air advection over the Northern Pacific and Atlantic oceans and the large-scale subsidence over the southern Indian Ocean are well reproduced by the model, there are some significant differences from the observed field of r_w. Among these differences are (1) the lack of dryness off the west coasts of California in January and South America during July, as already noted in reference to Figures 3 and 4. The differences between the model and SMMI distributions

TABLE 1. Sea Surface Temperature (SST)(K), Precipitable Water (kg m^{-2}), and the Greenhouse Effect ($\mathcal{G}$)

T_SK	w,kg m^{-2}	$\mathcal{G}$
272.00	...	1.41
274.00	10.7	1.43
276.00	11.5	1.46
278.00	12.1	1.47
280.00	13.9	1.48
282.00	17.0	1.50
284.00	17.6	1.52
286.00	18.4	1.52
288.00	18.4	1.53
290.00	19.7	1.53
292.00	21.6	1.54
294.00	24.0	1.54
296.00	28.0	1.55
298.00	32.1	1.56
300.00	39.2	1.59
302.00	47.3	1.62
304.00	...	1.66

of PWC in these regions account for the larger model values of PWC in the SST range 288 K < SST < 300 K. These differences are similar to the differences noted by *Liu and Tang* [1992] between the SSMI and the ECMWF fields of PWC. A possible explanation for the discrepancy between the model and the retrieved PWC in these regions is that the subsidence in the model in these subtropical areas is too weak and the boundary layer is deeper than might be expected. (2) We might interpret the results of Plate 2*a*, in comparison to Plate 1*a*, that the model overpredicts the amount of water vapor convergence poleward of about 45° S during January. The tendency of the model is to predict too much moisture throughout the troposphere, and especially in the middle troposphere, in these regions for both hemispheres compared to ECMWF FGGE level 2 B data. This difference is noted in *Randall et al* [1985, Figure 14 of that paper] and the effect of this discrepancy on the greenhouse effect is discussed later. (3) There is a lack of dryness in the model associated with the wintertime subsidence in the southern hemisphere. While the model predicts drier air associated with the subsidence over the Indian Ocean, this dryness does not extend as far across the southern Pacific Ocean as it does in the observations.

5. Clear Sky Greenhouse Effects

5.1. Clear Sky Emission to Space

An understanding of the relationship between the longwave emission to space and the surface temperature of the planet is central to the treatment of water vapor feedback in simple models of the Earth's climate system [e.g., *North et al.*, 1981]. At the core of these studies is the famous *Budyko* [1969] relationship

$$I = A + BT_s, \tag{2}$$

where we use T_s to represent the SST and I is the all sky emission to space. This relationship is used in simple climate models to study climate change induced by a perturbation forcing. In these models, B is the key parameter that defines the strength of the feedback and the time scale of the adjustment back to equilibrium by perturbed systems. In the present study we examine (2) in the context of changes of clear sky emission only, namely, I_{clr}, and T_s.

Figure 5 is a graphical depiction of the relationship between the clear sky emission I_{clr} and the T_s, as predicted by the GCM for 24 months of simulation and as derived from 12 months of ERBE satellite observations over the oceans. The clear sky emission predicted by the GCM is represented by the solid curves, in the manner discussed for previous diagrams. The behavior of I_{clr} as a function of T_s, both for the model and the observations, is distinctly different than that predicted by the Budyko formula over the entire range of SSTs considered. The results do suggest that the emitted radiation is broadly linear in SST over the range $T_s < 288$ K, but they also suggest that I_{clr} is insensitive to SST for $T_s > 298$ K. The GCM appears to underpredict the emitted radiation over the first of these temperature ranges, suggesting that the greenhouse effect in the model for these regions is too strong, despite the fact that the agreement in the PWC is relatively good for these temperatures (Figure 3).

We arbitrarily divide both the GCM and the ERBE data into these two SST regimes and carry out a linear least-squares fit to I_{clr} for each. The coefficients obtained from these fits are provided in Table 2. The coefficients derived from the GCM fields are remarkably close to those derived from the ERBE data for $T_s < 288$ K but differ from the ERBE coefficients for $T_s > 288$ K, although the model does produce the right qualitative differences between the two temperature regimes.

5.2. Clear Sky Greenhouse Effect and Its Relation to Precipitable Water Content (PWC)

An interpretation of the following greenhouse parameter

$$\mathcal{G} = \sigma T_s^4 / I_{clr} \tag{3}$$

is given in part 1. It is also demonstrated in part 1 how $\mathcal{G}$ varies in an approximately linear way with the precipitable water content when clear sky values of I are used in its definition. Figure 6*a* presents an example of this relationship derived from data composited for the 1988/1989 DJF and 1989 JJA seasons using clear sky values of I_{clr} obtained from ERBE data and coincident precipitable water data derived from SSMI measurements. These results essentially reproduce the earlier results of part 1 derived from different data (Nimbus 7 ERB and SMMR observations). The mean relationship derived from the scatter of points is also given in Table 1. The scatter about the mean relationship between $\mathcal{G}$ and PWC, which we refer to as climatology and which is not shown on the diagram, results from a number of factors, including variations in the vertical distributions of temperature and water vapor (part 1). For example, a profile with enhanced levels of vapor in the upper troposphere, relative to a given climatology, is characterized by decreased emission to space and thus values of $\mathcal{G}$ in excess of the climatological values. Conversely, reduced levels of upper tropospheric moisture, such as occur in local regions of subsidence, are associated with lower values of $\mathcal{G}$. This effect has also been confirmed in a different way in the recent study of *Ackerman et al.* [1992]. Thus the departure of local values of $\mathcal{G}$ from those expected from the climatological $\mathcal{G}$–w relationship provides an indication of the impact of large-scale motion on the greenhouse effect through the influence of the former on the water vapor distribution.

The relationship between $\mathcal{G}$ and PWC given in Figure 6*a* by the scattered pluses is reproduced in Figure 6*b*, to-

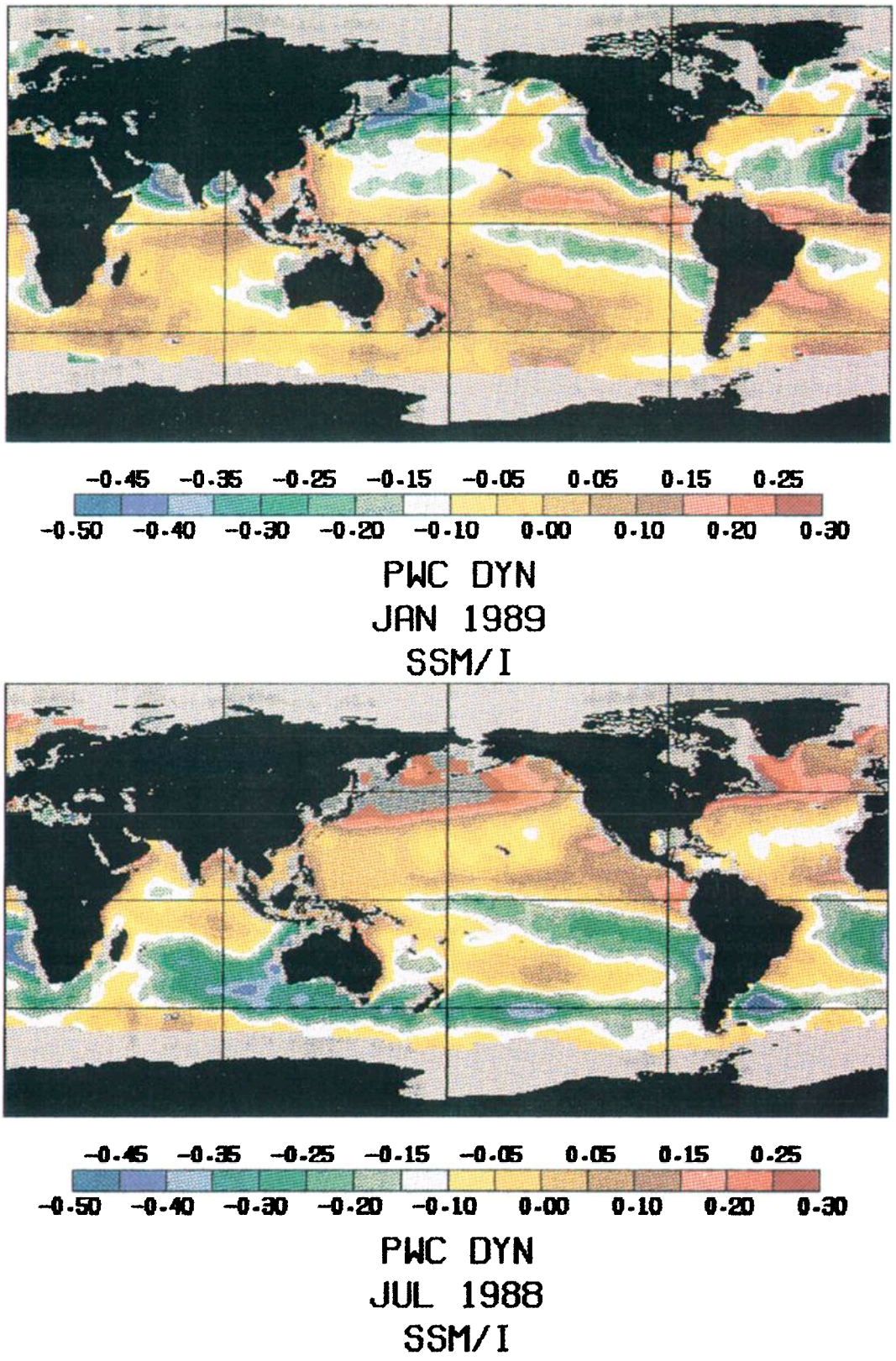

Plate 1. Distributions of r_w for (*a*) January and (*b*) July derived from SSMI PWC–SST data.

gether with the equivalent relationship derived from the GCM which is presented by the solid curves. The model predicts a slightly different slope in this relationship and simulates a stronger greenhouse effect in those regions defined by PWC<20 mm. This difference provides another way of demonstrating the lower emissions in regions defined by SSTs less than 288 K in Figure 5. An explanation for these differences is tied to the explanation of the differences in r_w noted above, namely that the model has too much upper tropospheric moisture at these latitudes despite the

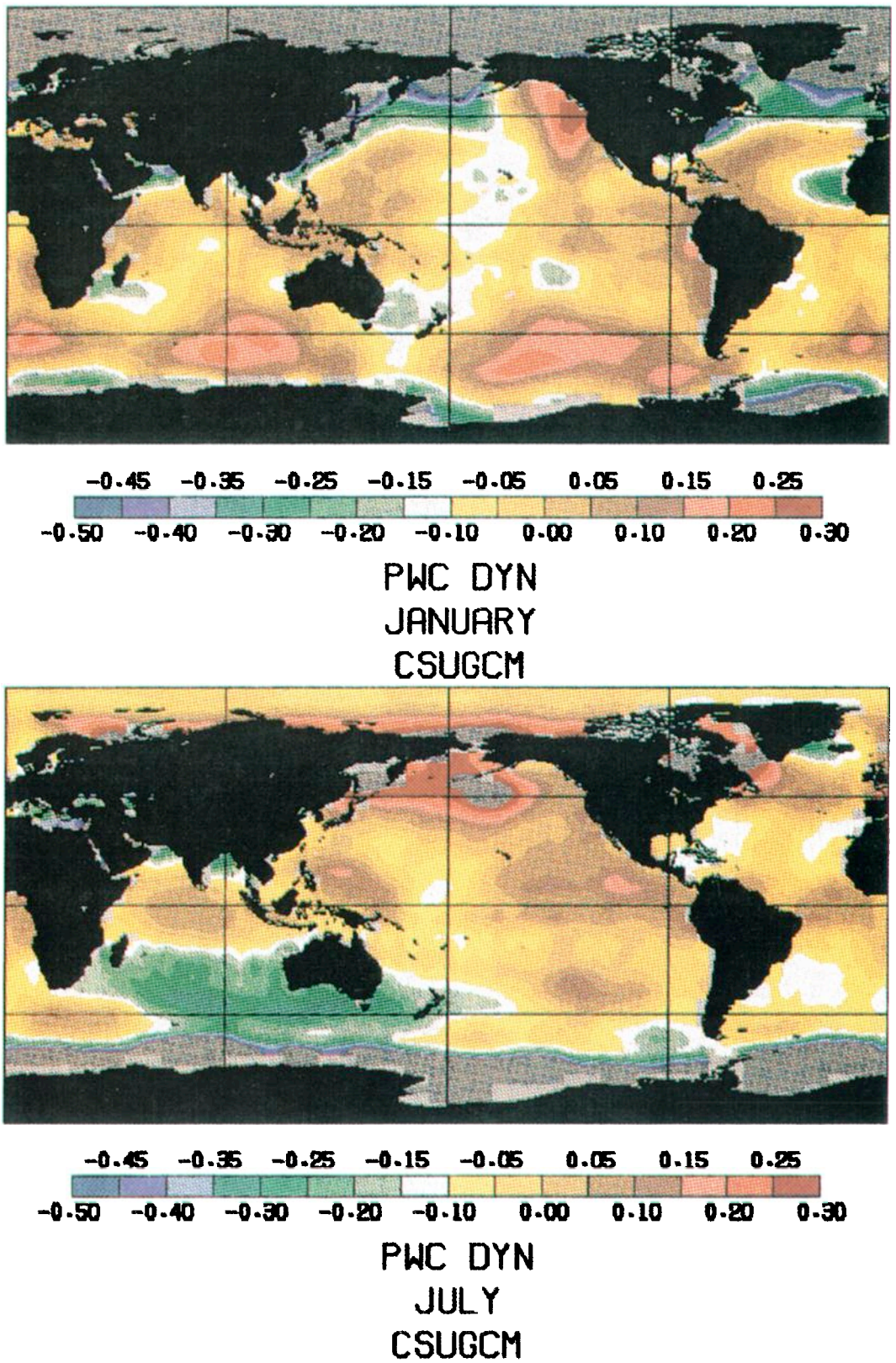

Plate 2. Same as Plate 1(*a*) and 1(*b*) but for the r_w derived from GCM PWC.

relatively good agreement between the simulated and the observed values of PWC in these regions.

It is argued that the departure of local values of $\mathcal{G}$ from those expected from the climatological $\mathcal{G}$–w relationship, which is also listed in Table 1, provides an indication of the impact of large-scale motion on the greenhouse effect through the effects of the vertical distribution of water vapor on $\mathcal{G}$. A convenient parameter to consider in this regard

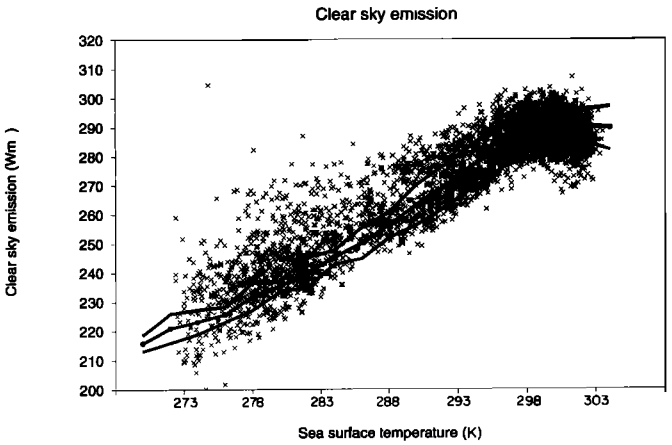

Fig. 5. Clear sky longwave radiation as a function of SST. Symbols apply to ERBE observations; the middle curve is the average of the GCM simulations.

TABLE 2. Observed and Modeled Parameters Defining the Emitted Radiation to the Sensitivity of the Earth's Greenhouse Effect to Changing SST

Parameter	Temperature	ERBE	CSU-GCM
A, Wm^{-2}	$T_s < 25°C$	223.6	219.8
B, Wm^{-2} K^{-1}		2.57	2.56
A, Wm^{-2}	$T_s > 25°C$	311.0	284.7
B, Wm^{-2} K^{-1}		-0.86	0.18
Parameter	**Temperature**	**ERBE/SSMI**	**CSU GCM**
a	...	1.348	1.422
b, mm^{-1}	...	0.066	0.0044
c, K^{-1}	...	0.0686	0.0561
d, mm	...	18.	19.
g, K^{-1}	...	0.012	0.006

ERBE, Earth Radiation Budget Experiment; CSU, Colorado State University; GCM, general circulation model; SSMI, special sensor microwave imager.

is

$$r_{\mathcal{G}} = \frac{\mathcal{G}_{\text{local}} - \mathcal{G}_{\text{clim}}}{\mathcal{G}_{\text{local}}} \tag{4}$$

where $\mathcal{G}_{\text{local}}$ is the value of $\mathcal{G}$ derived from local values of T_s and I and $\mathcal{G}_{\text{clim}}$ is the value of $\mathcal{G}$ deduced from the local value of w and the climatological $\mathcal{G}$–w relationship interpolated from the data given in Table 1.

Plates 3*a* and 3*b* present the global distributions of $r_{\mathcal{G}}$ obtained from ERBE-SSMI observations for January 1989 and July 1988, respectively, and Plates 4*a* and 4*b* present the corresponding distributions of $r_{\mathcal{G}}$ derived from the January and July GCM output. The distributions in Plates 3*a* and 3*b* clearly show the effects of large-scale subsidence on $\mathcal{G}$. Areas of subsidence are characterized by negative values of $r_{\mathcal{G}}$ and these areas are found in the regions associated with the descending branch of the Hadley circulation and the regions of subsidence on the eastern flank of the circulation around the subtropical high-pressure regions.

Broad similarities exist between the observed fields of $r_{\mathcal{G}}$ and the model-derived fields of this quantity. Negative values of $r_{\mathcal{G}}$ associated with regions of subsidence and with lower levels of upper tropospheric moisture which were identified previously in Figures 2*a*-*d* exist along the eastern edge of the southern Pacific and Atlantic oceans for both months.

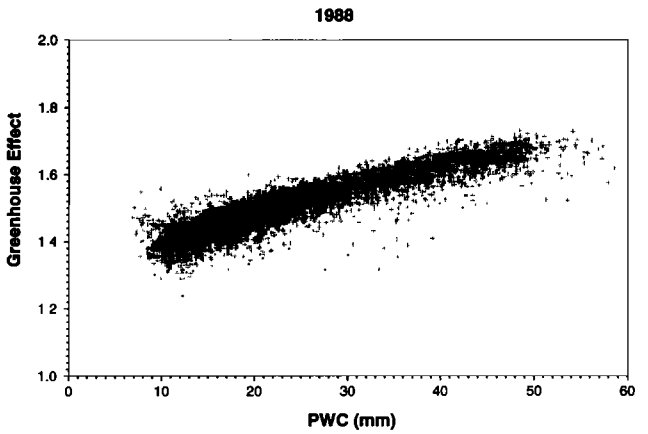

Fig. 6*a*. Clear sky greenhouse parameter as a function of PWC. The observations correspond to 12 months of coincident Earth Radiation Budget Experiment (ERBE) and SSMI data from February 1988 to January 1989.

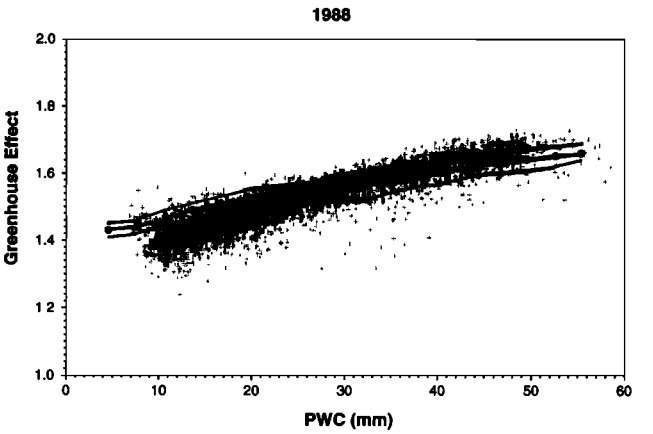

Fig. 6*b*. Comparison of the simulated and observed clear sky greenhouse parameter as a function of PWC.

Regions of a reduced greenhouse effect due to lower levels of upper tropospheric moisture extend across the equatorial Pacific slightly north of the equator during January and south of the equator during July in a manner similar to the patterns described in relation to the TOVS brightness temperature distributions. An important difference between the model and observed fields of $r_{\mathcal{G}}$ is the tendency of the former to overpredict the clear sky greenhouse in the middle–to–high latitudes of the summer hemisphere. This explains the tendency noted in reference to Plate 4*b* of the model to overestimate the greenhouse effect when PWC< 20 mm.

5.3. An Analysis of the Sensitivity of $\mathcal{G}$ to Sea Surface Temperature (SST)

Figures 7*a* and 7*b* provide plots of $\mathcal{G}$ as a function of SST. The observed relation given by the scatter of points in Figure 7*a* also resembles that described in part 1 with an enhanced greenhouse effect occurring over the oceans where the temperature is warmer than 300 K. In part 1 we fit the relationship shown in Figure 6 according to

$$\mathcal{G} = a + bw \tag{5}$$

where w is the PWC and for the present purposes we express this as [*Stephens*, 1990]

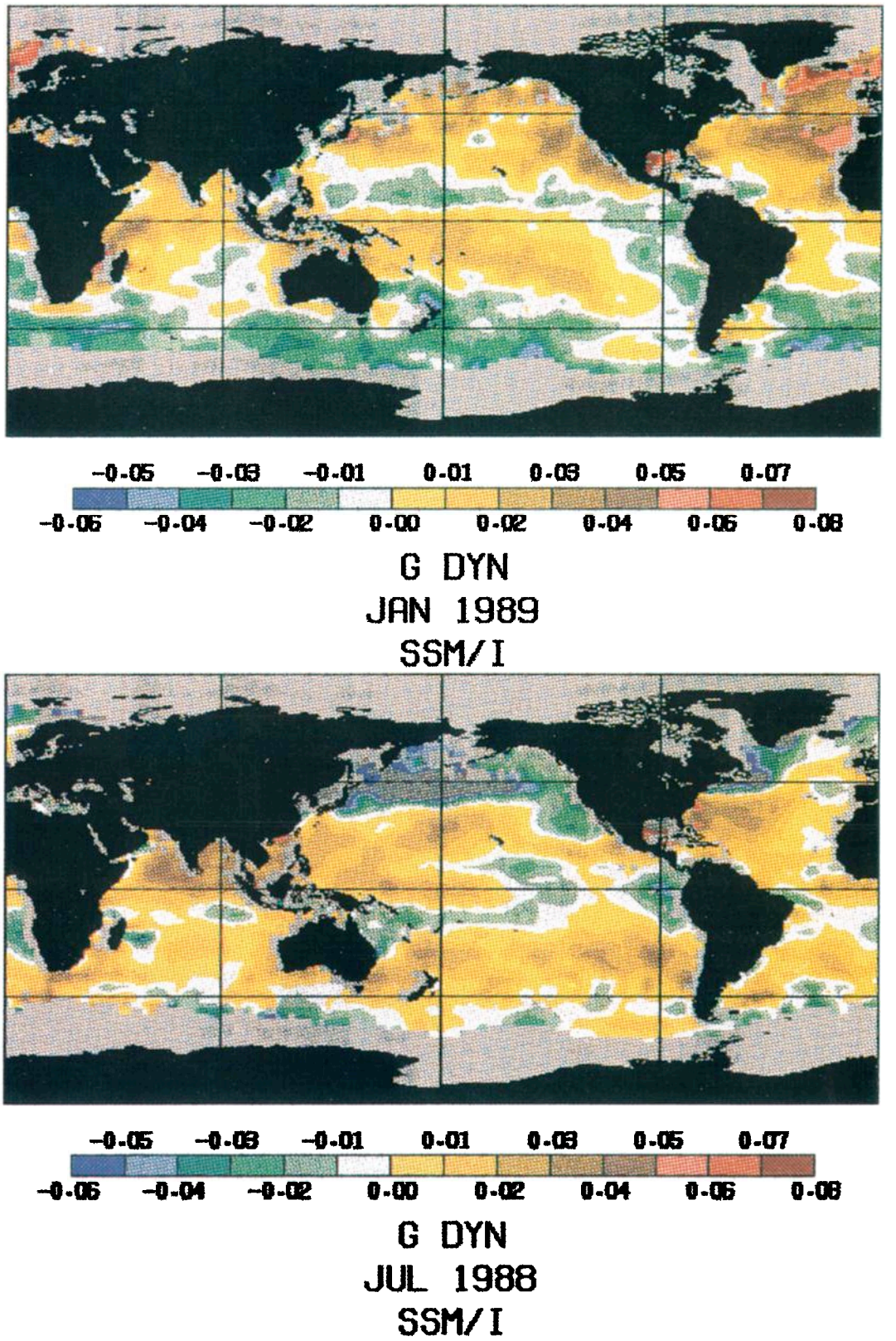

Plate 3. Distribution of r_g derived from ERBE and SSMI observations for (*a*) January and (*b*) July.

$$w = d\exp[c(T_s - 288)]. \quad (6)$$

Combining these relationships yields

$$\mathcal{G} = a + bd\exp[c(T_s - 288)] \quad (7)$$

and the relationships predicted by (9), with coefficient values derived from least squares fit of both the GCM and the satellite data shown above in Figures 3 and 6, are presented in Plate 3. Values of a, b, c, and d derived from these fits are also listed in Table 2.

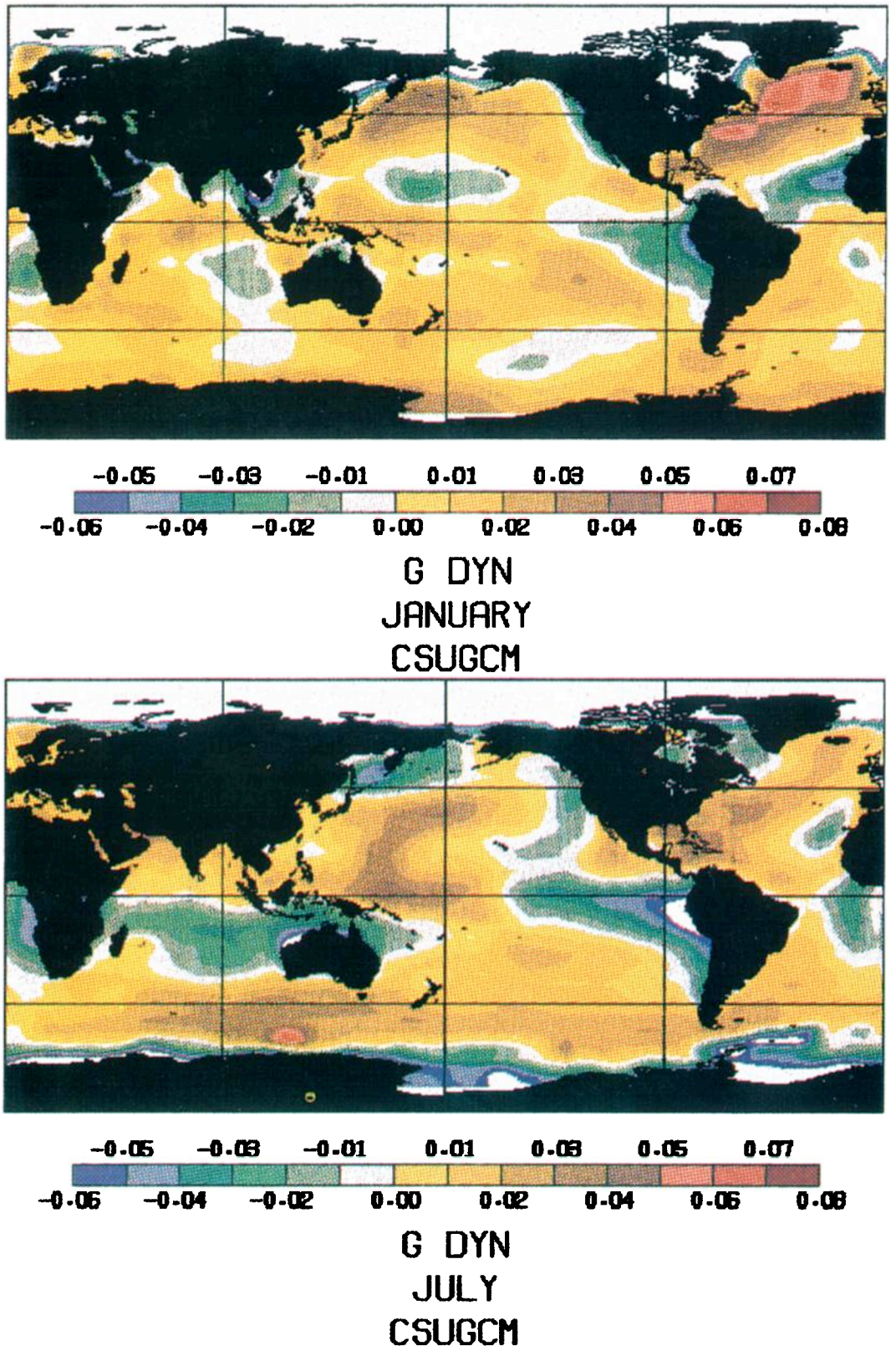

Plate 4. Same as Plate 3 but for $r_{\mathcal{G}}$ derived from model values of $\mathcal{G}$.

From the definition of $\mathcal{G}$ that follows from the combination of (5) and (6), we define

$$g = \frac{d\mathcal{G}}{dT_s} = bdc\exp[c(T_s - 288)] \quad (8)$$

which establishes the sensitivity of the greenhouse effect to changes in SST. As an illustration, let us assume that the global mean SST is 292 K, then g= 0.006 K^{-1} using model-derived values of b, d and c compared to g=0.012 K^{-1} from the observations. Therefore, the model underestimates the

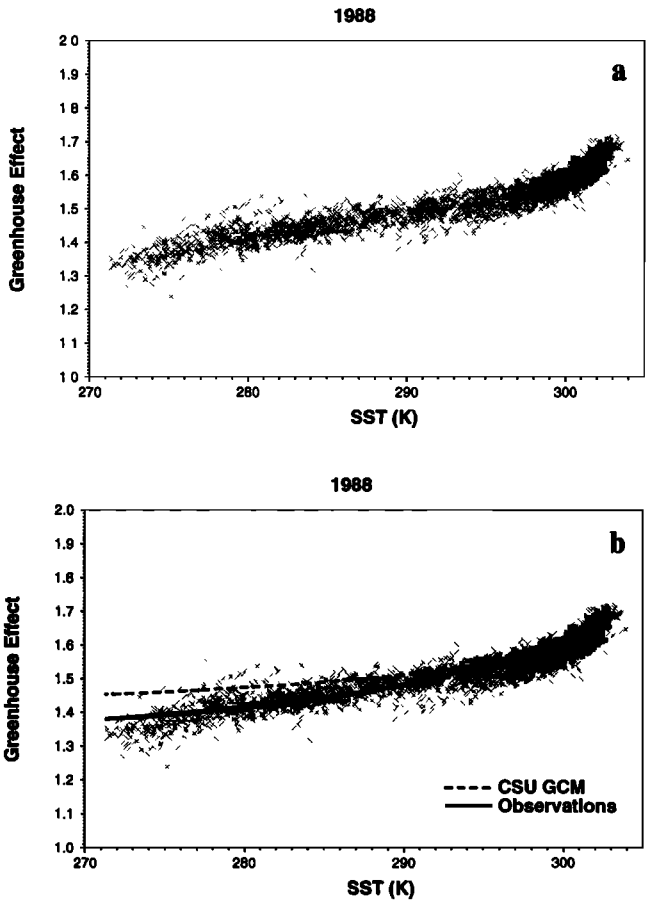

Fig. 7. (*a*) $\mathcal{G}$ as a function of SST and (*b*) comparison of modeled and observed relationship between $\mathcal{G}$ and SST. The solid curve labeled observations is the relationship fitted according to equation (9) with parameter obtained from observations.

sensitivity of the greenhouse to changes in SST. This underestimate arises from the lack of water vapor over warmest SSTs in the model producing smaller values of c combined with the enhanced greenhouse of the model over regions of colder SSTs producing lower values of b compared to observations.

The relationship (8) also establishes an important property of the Earth's greenhouse; that its sensitivity to changing SST is not uniform over the globe and is greatest over regions of warmest SSTs. Furthermore, (8) highlights the relevance of the slope of $\mathcal{G}$ as a function of PWC and the c factor in the exponent of (6) in dictating the magnitude of the sensitivity. The model, like the observations, also shows a general increasing trend in $\mathcal{G}$ with increasing SST, but it underpredicts the magnitude of this trend significantly. This is due in part to the problem of the model in simulating the PWC of the tropical atmosphere.

The sensitivity parameter defined above and estimated from the two data sets should not be misconstrued as a measure of feedback between $\mathcal{G}$ and the SST. It was noted in part 1 how many factors other than SST influence $\mathcal{G}$ and thus the parameter g. Among these factors are the vertical profiles of water vapor and temperature. The parameters used to estimate g in this study correspond to a set of conditions that do not remain fixed but vary in association with changing SST. A fundamental issue, and a topic of a further study, concerns the robustness of the relationship shown here and whether the same sensitivities derive from climate states that are different from the present-day state observed in this study.

5.4. *Seasonal Variability of the Greenhouse Effect*

In part 1 the relationship between the dimensionless measure of the clear sky greenhouse effect $\mathcal{G}$ and the infrared opacity over oceans

$$\mathcal{A} = \sigma T_s^4 - I_{\text{clr}} = \frac{\mathcal{G} - 1}{\mathcal{G}} \tag{9}$$

expressed in watts per square meter was discussed. In considering the seasonal variability of the greenhouse effect we consider the dimensional quantity $\mathcal{A}$ rather than $\mathcal{G}$. We anticipate that $\mathcal{A}$ undergoes a distinct seasonal cycle in association with the seasonal cycle of PWC since $\mathcal{A}$ is related to $\mathcal{G}$ and this, in turn, is related to PWC, as we have shown above. Figure 8 shows the seasonal correlations between the zonal averages of $\mathcal{A}$ over ocean regions derived from simulations and the ERBE observations. At each latitude, $\mathcal{A}$ is averaged zonally over the oceans and the average annual cycle of this zonal average is derived for the 2 years of model data and 4 years (1985–1988) of ERBE data. These annual cycles are correlated and the zonal distribution of these correlations are shown in Figure 8. The correlations are close to one within 40° of the equator and exceed 0.5 within 50° of the equator. The ERBE clear sky values become questionable poleward of 50°, because of the difficulty of distinguishing between clouds and snow or ice.

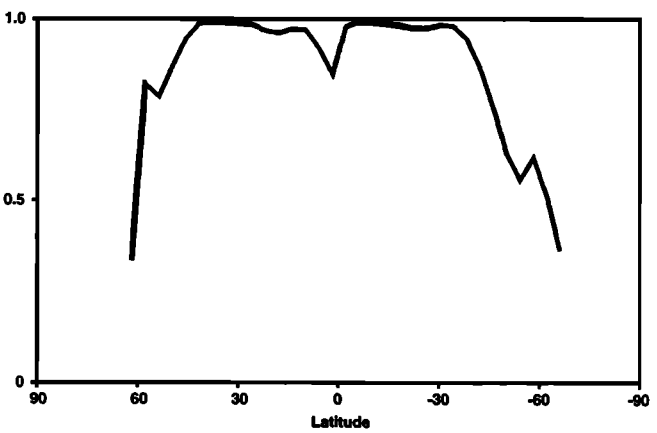

Fig. 8. The correlation coefficient between the observed and the model-derived zonal average (over oceans) of the annual cycle of the infrared opacity of the atmosphere $\mathcal{A}$ as a function of latitude.

Plate 5*a* shows maps of the July seasonal anomaly for the clear-sky infrared opacity, for the observations (top) and the simulation (bottom). Corresponding results for January are presented in Plate 5*b*. The pattern of the observed seasonal anomaly is very well simulated by the model, for both months, although the amplitudes of the anomalies are smaller than observations in some places, such as in the western North Atlantic and the Gulf of Mexico in July. The agreement in the seasonal anomalies of $\mathcal{A}$ derived from the model and from ERBE data is to be expected since the model is driven by prescribed SSTs and the monthly anomalies of PWC are also broadly defined by anonamlies of SST.

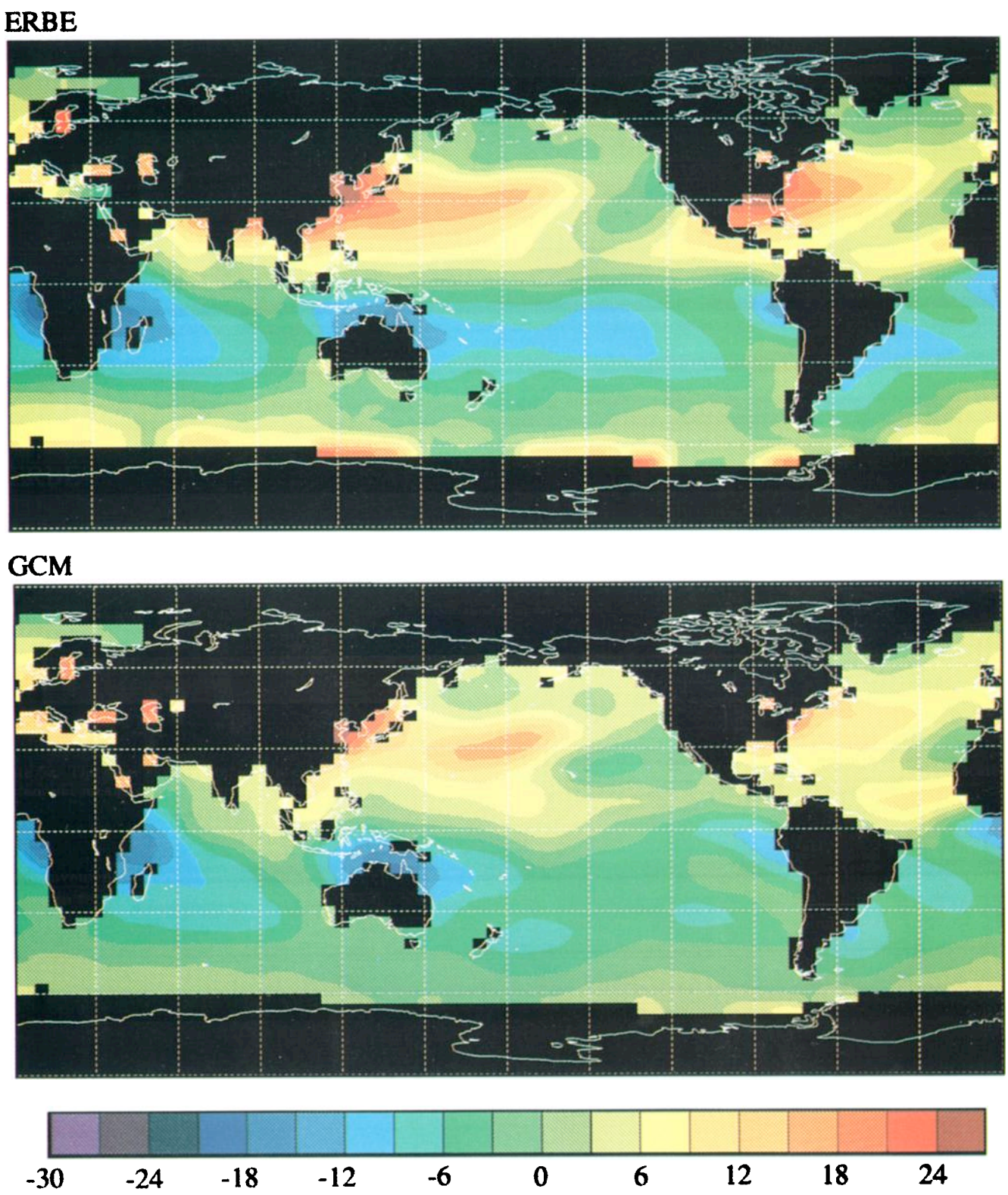

Plate 5a. The clear sky July opacity anomaly (July mean minus the annual mean) derived from an average of 4 years of ERBE data (top) and 2 years of GCM data (bottom) panel. Color scale in watts per square meter.

6. CLOUDY SKY EFFECTS

A convenient way of studying the effects of clouds on the ERB is in terms of the following top of the atmosphere flux quantities:

$$C_{LW} = I_{\mathrm{clr}} - I_{\mathrm{obs}}, \tag{10a}$$

$$C_{SW} = Q_o(\alpha_{\mathrm{clr}} - \alpha_{\mathrm{obs}}). \tag{10b}$$

In these definitions, I_{clr} and α_{clr} are the longwave flux emitted to space and the albedo of the planet under clear skies;

January Clear-Sky Greenhouse Anomaly

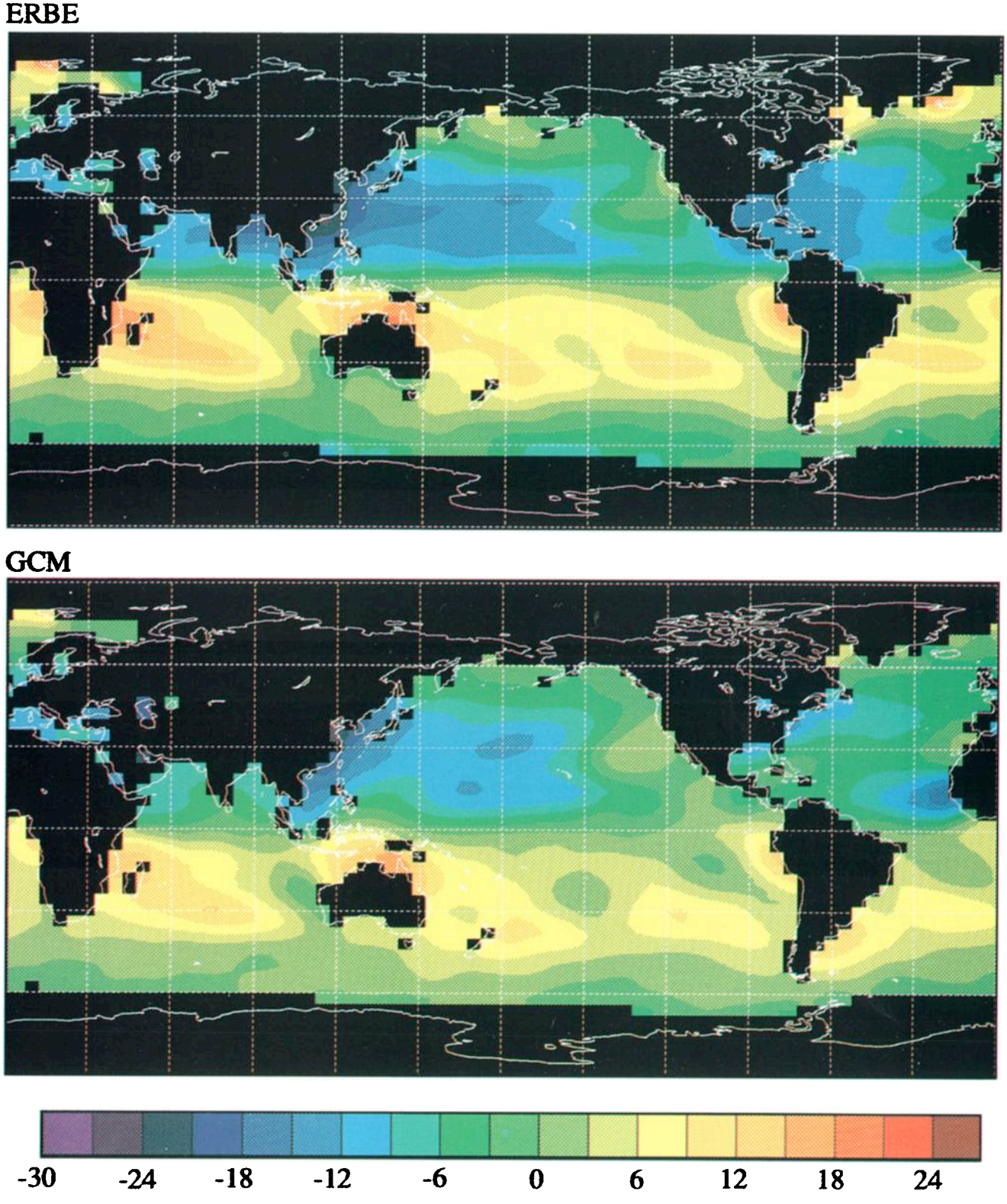

Plate 5*b*. Same as for Plate 5*a* but for January.

I_{obs} and α_{obs} are the observed flux and albedo (clear plus cloudy sky values); and Q_o is the solar insolation on a horizontal surface at the top of the atmosphere. The interpretation of C_{LW} and C_{SW} is given in Part II among other references. Here we present comparisons of C_{LW} and C_{SW} and the albedo quantity $\Delta\alpha = \alpha_{obs} - \alpha_{clr}$ as a function of SST. It is reasonable to consider $\Delta\alpha$ as the albedo of clouds in the case of dark underlying surfaces like the ocean. Part 2

presents a slightly more elaborate method for estimating the cloud albedo from measured ERBE fluxes over bright surfaces, but we will use $\Delta\alpha$ here as indicative of cloud albedo since our analysis applies only to ocean areas.

6.1 The Relationship Between the Longwave and the Albedo Effects of Cloud to Sea Surface Temperature (SST)

As mentioned in part 2, C_{LW} provides a direct measure of the reduction of longwave radiation by absorption and emission of clouds in the atmosphere relative to clear skies. Figure 9 presents 12 months of C_{LW} derived from ERBE data as a function of SST and compares the same flux quantity derived from the CSU GCM. The general behavior of C_{LW} with SST is discussed in part 2, where it is noted that there appear to be two distinct regimes for this behavior: in one regime, C_{LW} decreases over much of the SST range varying from values of 40 W m^{-2} at $T_s \approx 273$ K to about 0-10 W m^{-2} at $T_s \approx 300$ K. The second regime occurs over water warmer than about 300 K, where C_{LW} dramatically increases to values near 80 Wm^{-2}. This behavior is partly indicative of the increased cloudiness both equatorward and poleward of the subtropics, which are indicated on this diagram by the minimum in C_{LW}, and partly a result of the changing macroscopic properties of clouds in these regions where cold deep clouds prevail over the warmer equatorial regions and give rise to the largest values in C_{LW}. The comparison between the simulated relationship and that observed suggests that these two regimes are actually well simulated by the model although the magnitudes of C_{LW} over the warm ocean regime are larger than observed and slightly smaller than observed over colder waters. Two possible sources for the discrepancy over the warmest SSTs may be related to specific assumptions in the model regarding how clouds are treated. The assumption that anvil clouds radiate as a black-body together with the assumption that clouds completely fill the grid box will exaggerate the model values of C_{LW} over the warm SST regions.

Figures 10*a* and 10*b* present January and July values of C_{SW} as a function of SST. Values for each hemisphere are shown separately to highlight the complicated variation of C_{SW} with SST. The solar fluxes reflected by the summer hemisphere clouds vary with SST in a way that resembles the two regimes noted for C_{LW}, except that C_{SW} increases from about -150 Wm^{-2} for the colder SSTs (and thus at higher latitudes) due to the reflection from the summertime clouds located in the mid- to high-latitude storm tracks. C_{SW} increases to near zero over the subtropics, followed by a sharp decrease associated with the bright clouds of the warmer equatorial oceans. The behavior of C_{SW} in the winter hemisphere poleward of the subtropics differs from that just described for the summer hemisphere. In the former case, the variation of C_{SW} with SST is a result of the product of two factors that have opposing variations with latitude: one is the decreasing insolation and the other is the increasing albedo with increasing latitude. The latter, in turn, is a result of both increasing cloudiness poleward of the subtropics and the decreasing solar elevation with increasing latitude. Both factors contribute to an increase in the albedo of cloud from the subtropics to mid-latitudes, as we show below. The two factors, that of an increased albedo and that of a decreasing solar flux, combine to produce a variation in C_{SW} that starts near zero for clouds at high latitudes and decreases to a minimum of -50 Wm^{-2} at approximately T_s =293 K, followed by an increase toward zero and then a rapid falloff with increasing SST, similar to that noted for the summer hemisphere.

Figures 11*a* and 11*b* present January and July values of $\Delta\alpha$ as a function of SST. The remarkable feature of these diagrams is how the different hemispheric behavior of C_{SW} maps onto one broad and apparently well-defined relationship. The albedo parameter $\Delta\alpha$ has a minimum over the subtropics where there is a minimum in cloudiness, and increases both equatorward and poleward of these clear sky

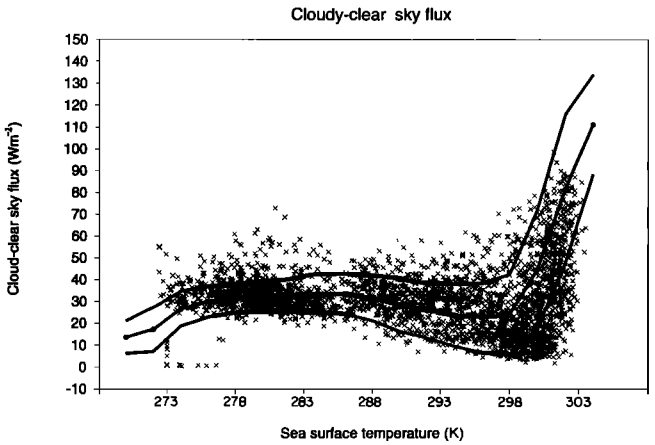

Fig. 9. C_{LW} as a function of SST.

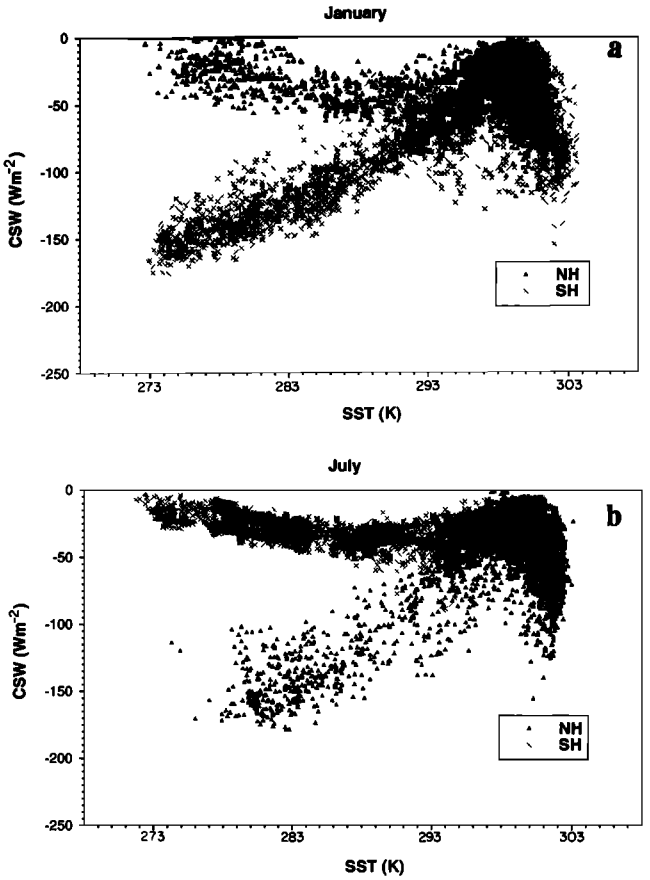

Fig. 10. C_{SW} as a function of SST for (*a*) January and (*b*) July. C_{SW} is separated by hemisphere to illustrate the effects of the seasonal change in insolation on C_{SW}.

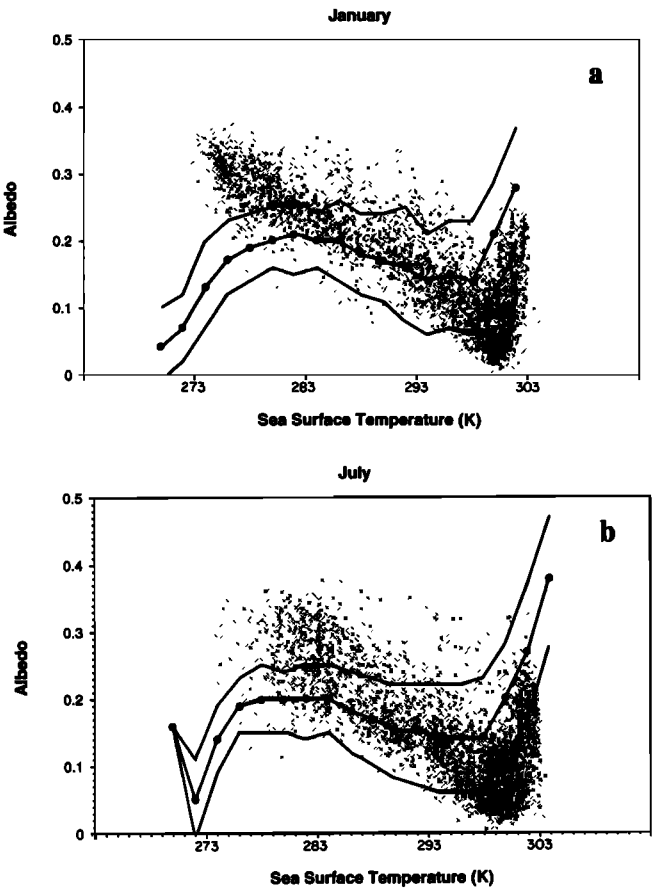

Fig. 11. Cloud albedo parameter $\Delta\alpha$ as a function of SST for (*a*) January and (*b*) July.

regions. The SST–$\Delta\alpha$ relationships obtained from the GCM are also given on these diagrams for comparison. The model behavior of $\Delta\alpha$ with SST broadly follows the observed behavior, although there are significant differences between the two sets of data. The cloud albedo predicted by the model exceeds that observed in the equatorial warm ocean regions but is much too low for the mid-latitude clouds over regions characterized by $T_s < 285$ K. These features may be due to either poorly modeled cloud amount, poorly specified cloud albedo, or a combination of both (note that $\Delta\alpha$ is a hybrid of both factors). Comparisons conducted by *Harshvardhan et al.* [1989] between the total cloudiness of the model versus the ISCCP total cloudiness reveals that the model tends to overpredict cloudiness in the subtropics (hence the larger values of $\Delta\alpha$ at temperatures near 300 K), slightly underpredicts the total cloudiness in the equatorial regions and greatly overestimates the cloudiness in the summer mid-latitudes. This suggests modeling problems both with the parameterization of cloud albedo in the equatorial region and with the estimation of the effect of cloud amount on the subtropics and higher latitudes on albedo.

6.2. The Seasonal Cycle of the (CRF)

Seasonal changes in ERBE values of C_{LW}, C_{SW}, and C_{net} are discussed by Cess et al. (1992) and a comparison of the model and observed seasonal variations of these quantities is described by *Randall and Tjemkes* [1991]. These comparisons are not repeated here. Instead we show the temporal correlations of the simulated and observed seasonal responses of the zonally averaged solar, terrestrial, and net cloud radiative forcing in Figure 12. Unlike for Figure 8, these correlations are of zonally averaged (land plus ocean) fluxes. The correlations are generally close to one in the subtropics. The correlation between the net flux is significantly less than unity in the tropics where small differences in C_{net} distort these correlations since C_{net} is near zero owing to cancelling contributions by C_{LW} and C_{SW}. As discussed by *Randall and Tjemkes* [1991] and *Cess et al.* [1991], the seasonal response in the tropics is dominated by the shift of the intertropical convergence zone (ITCZ) between hemispheres, following the Sun and this is well simulated by the model despite the correlations shown [e.g., *Randall and Tjemkes*, 1991]. In middle latitudes, however, the correlations between the simulation and the observations are considerably smaller and even become negative, particularly in the northern hemisphere. Evidently, the model does not correctly simulate the seasonal change of the cloud forcing in these latitudes. The changes are characterized by deep convection over land primarily in the spring and summer and strong storm-track cloudiness over the oceans, particularly in winter. The particular reasons for these problems require further study.

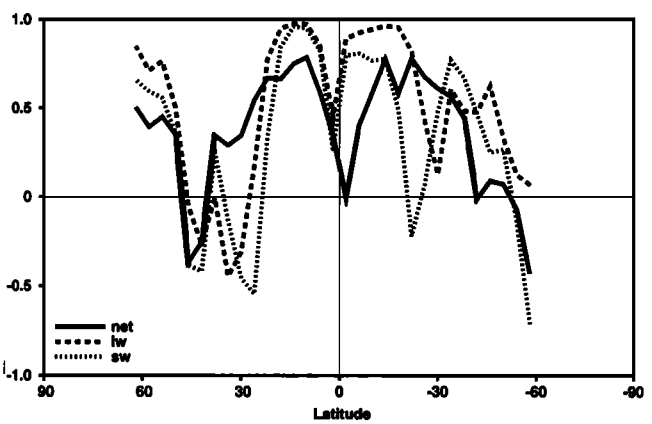

Fig. 12. The correlation coefficient between the observed and the model-derived zonal averages (land plus oceans) of the annual cycle of C_{LW}, C_{SW}, and C_{net} as a function of latitude.

7. SUMMARY AND CONCLUSIONS

The main aim of the study reported in this paper is to provide a limited test of how well the CSU GCM treats particular interactions between aspects of its hydrological cycle and model parameterizations of radiative processes. Two broad types of tests of the model are introduced to study these interactions. The first type of test focuses on comparing various sensitivity relationships established in the model with those observed on Earth. These relationships are considered basic to our understanding of different feedbacks that are thought to operate in the climate system. The second type of test focuses on comparison of the seasonal cycle of selected quantities. Both are proposed as important tests of the model since they represent, on the one hand, key sensitivities of physical linkages and, on the other hand, tests of response to changing external forcing. If a model cannot simulate either the sensitivity relationships described in this

paper or the seasonal cycle of these parameters then it lacks credibility as a tool for studying global climate.

The specific sensitivity relationships examined in this paper are those among PWC, cloud albedo, and cloud radiative forcing as a function of sea surface temperature. We also investigate the simulated and observed response of the greenhouse effect and cloud radiative forcing to seasonal forcing. The main results of this study are: (1.) Despite the detailed differences noted below, the CSU GCM, which we take to be representative of the current generation of GCMs, is able to simulate some aspects of the observed sensitivities fairly well. Qualitative successes of the simulations include realistic variations of PWC with SST, the clear sky greenhouse parameter and its variation with both PWC and SST, and cloud longwave radiative forcing with SST, as well as the seasonal changes of the precipitable water and the cloud radiative forcing. (2.) Whereas there is qualitative agreement, there are many serious quantitative differences between the model and the observations. Notable problems in the simulations include an underprediction of the PWC in the tropics and an excessively strong clear-sky greenhouse effect in the mid-latitudes, which we propose to be due to excessive upper tropospheric PWC during winter. These differences combine in such a way that the model underestimates the clear-sky greenhouse effect–SST sensitivity compared to that derived from observations. This might suggest the possibility of a weaker than actual water vapor feedback mechanism in the model. Such a model is likely to give a conservative estimate of global warming. (3.) The simple analysis of the clear-sky greenhouse effect and its sensitivity to changes in SST described in this paper illustrates how this sensitivity non-linearly varies with SST with the greatest sensitivity occurring over the warmest SSTs. This is in direct contrast to the simple analysis of water vapor feedback that is often described in terms of the Budyko sensitivity parameter B in (2) which is taken to be a global quantity. Both model and observations of B are shown to agree closely in this study, whereas the greenhouse sensitivity does not. This result further demonstrates the inappropriateness of the simple linear-in–SST relationship of Budyko for the emitted radiation from the clear sky planet, let alone for a cloudy sky, and how this oversimplification fails to represent the Earth's clear sky greenhouse effect and its variation with changing SST. (4.) Differences between the simulated and observed radiative properties of clouds include the overprediction of the longwave cloud radiative forcing over warm tropical oceans and a significant underestimate of the cloud reflection in mid-latitudes during the summer season.

These results can be used to address two questions. First, to what extent is the present model a credible tool for simulating the complex feedbacks that determine climate change in response to external forcing? We have shown that the model qualitatively simulates the observed sensitives of climatically important parameters such as the clear sky greenhouse parameter and the cloud radiative forcing to sea surface temperature, to dynamical perturbations, and to seasonal change. On the other hand, the serious quantitative differences force us to conclude that this model, and perhaps most other models, give at best, only qualitative guidance on the response of the climate system to external perturbations.

Second, we can use our results to ask how the results of the model can be improved. Incorporation of convective downdrafts, for instance, may improve the realism of the simulated tropical PWC. Partial cloudiness and a physically based relationship between predicted cloud water/ice concentrations and cloud optical properties may improve the simulation of the cloud radiative forcing. Our comparisons between the model and the observations suggest that these two model-development efforts, among others, can produce physically important improvements in the model results, that will permit more reliable simulations of climate sensitivity.

The conclusions of this work apply only to one GCM, although the degree of realism found is probably typical of other present-day GCM's. It is clearly important to test other models in the way the CSU GCM has been tested in this paper. Furthermore, it would be useful to examine the ability of models to simulate observed climatic anomalies and to examine how the sensitivity relationships described in this paper change in states of anomalous climate. A recent simulation made possible by the Atmospheric Model Intercomparison Project where the models are forced by observed SSTs may provide a suitable data set for such studies.

Acknowledgments. This research has been supported by NASA's Climate Program under grants NAG 5-1058, NAG-1-1266, and NAG-1-8876, by the U.S. Department of Energy under contract DOE-FG02-89ER69027, by the National Science Foundation under grant ATM-8907414, and by NOAA Climate Change Program NA90AA-D-AC822. Computing resources have been provided by the Numerical Aerodynamic Simulation Facility at NASA Ames. The authors also gratefully acknowledge the efforts of John Bates and X.(Fred) Wu of NOAA's Climate Research Division ERL in supplying them with the TOVS data used in this study.

REFERENCES

Ackerman, S., R. Frey and W. L. Smith, Radiation budget studies using collocated observations of AVHRR, HIRS/2, and ERBE instruments, *J. Geophys. Res.*, *97*, 11,513-11,525, 1992.

Arakawa, A., and W. H. Schubert, The interaction of a cumulus cloud ensemble with the large-scale environment, I, *J. Atmos Sci.*, *31*, 674-701, 1974.

Budyko, M.I., The effect of solar radiation variations on the climate of the Earth, *Tellus*, *21*, 611-619, 1969.

Cess, R. D., E. F. Harrison, P. Minnis, B. R. Barkstrom, V. Ramanathan, and T. Y. Kwon, Interpretation of seasonal cloud-climate interaction using Earth Radiation Budget Experiment data, *J. Geophys. Res.*, 97, 7613-7617, 1992.

Cheng, M.-D., and A. Arakawa, Inclusion of convective downdrafts in the Arakawa-Schubert cumulus parameterization, paper presented at the Indo-U.S. Seminar on Parameterization of Sub-Grid Scale Processes in Dynamical Models of Medium Range Prediction and Global Climate, Dep. of Sci. and Technol. Govt. of India, Natl. Sci. Found., Wash., D.C., 6-10 August, 1990, Pune, India, 1991

Harrison, E. F., P. Minnis, B. R. Barkstrom, V. Ramanathan, R. D. Cess, and G. G. Gibson, Seasonal variation of cloud radiative forcing derived from the Earth Radiation Budget Experiment, *J. Geophys. Res.*, *95*,18,687–18,703, 1990.

Harshvardhan, D. A. Randall, T. G. Corsetti, and D. A. Dazlich, Earth radiation budget and cloudiness simulations with a general circulation model, *J. Atmos. Sci.*, *46*, 1922-1942, 1989.

Hollinger, J., R. Lo, C. Poe, R. Savage, and J. Pierce, *Special sensor microwave/imager user's guide*, report, Naval Research Laboratory, Washington, D. C., 1987.

Liu, T. W., and W. Tang, Precipitable water and surface humidity over the global oceans from the SSM/I and ECMWF, *J. Geophys. Res.*, *97*, 2251-2264, 1992.

McMillan L.M., and C. Dean, Evaluation of a new operational technique for producing clear radiances, *J. Appl. Meteorol.*, *21*, 1005-1014, 1982.

North, G. R.,R. F. Cahalan, and J. A.Coakley, Energy balance climate models, *Rev. Geophys.*, *19*, 91-121, 1981.

Randall, D. A. and S. Tjemkes, Clouds, The Earth's radiation budget, and the hydrological cycle, *Palaeogeogr., Palaeoclimatol., Palaeoecol.*, *90*, 3-9, 1991.

Randall, D. A., J A. Abeles and T. G. Corsetti, Seasonal simulations of the planetary boundary layer and boundary-layer stratocumulus clouds with a general circulation model, *J. Atmos. Sci.*, *42*, 641-676, 1985.

Randall, D. A., Harshvardhan, and D. A. Dazlich, : Diurnal variability of the hydrological cycle in a general circulation model, *J. Atmos. Sci.*, 48, 40-61, 1991.

Reynolds, R. W., A real-time global sea surface temperature analysis, *J. Clim.*, *1*, 75-86, 1988.

Stephens, G. L., On the relationship between water vapor over the oceans and sea surface temperature, *J. Climate*,*3*, 634-645, 1990.

Stephens, G. L., and T. J. Greenwald, Observations of the Earth's Radiation Budget in relation to atmospheric hydrology, I, Clear sky greenhouse effect and water vapor feedback, *J. Geophys. Res.*, *96*, 15,311-15,324, 1991*a*.

Stephens, G. L. and T. J. Greenwald, Observations of the Earth's radiation budget in relation to atmospheric hydrology, II, Cloud effects and cloud feedback, *J. Geophys. Res.*, *96*, 15,325-15,340, 1991*b*.

Tjemkes, S. A., G. L. Stephens, and D. L. Jackson, Spaceborne Observations of Columnar Water Vapor: SSMI Observations and Algorithm, *J. Geophys. Res.*, *96*, 10,941-10,954, 1991.

Wu X., J.J. Bates and S.J.S. Khalsa, The Climatology of the Water Vapor Band Brightness Temperature from NOAA Operational Satellite, scheduuled to appear in *J. Climate*, July 1993.

D. A. Dazlich, D. A. Randall, G. L. Stephens, and I. L. Wittmeyer, Department of Atmospheric Science, Colorado State University, Ft. Collins, CO 80523.

S. A. Tjemkes, Institute of Meteorology and Oceanography, State University of the Netherlands, Utrecht, The Netherlands.

(Received May 4, 1992;
revised October 12, 1992:
accepted October 16, 1992.)